

Design and verification of low-friction and high-performance monotube magnetorheological damper

Weihan Li^{1,2,3,4} , Chengpei Zhou^{2,3,4},
 Guodong Bai^{2,3,4} and Xianxu 'Frank' Bai^{2,3,4} 

Abstract

The frictional force of the suspension damper is an essential factor affecting vehicle ride comfort. As an important basic component of intelligent suspension, magnetorheological (MR) damper has the advantages of simple structure and adjustable damping performance. However, the frictional force of the MR damper is excessively high, due to the high-pressure gas to avoid the cavitation effect. If the frictional force of MR damper can be reduced, the vibration isolation performance of the intelligent suspension based on the MR damper will be further improved. In this study, a monotube MR damper with low friction and high performance is proposed and investigated. Firstly, the structural design of the low-friction MR damper is carried out, and the mathematical model of its controllable damping force and uncontrollable damping force is established. Secondly, the key structural parameters of the MR piston are optimized, and the valve system is matched based on the optimized mechanical characteristics of the piston to avoid the cavitation effect. Thirdly, bench tests are carried out on the developed low-friction MR damper. The experimental results show that the frictional force of the MR damper is very low, and no cavitation effect occurs. Finally, the system performance simulation analysis is carried out on the 1/4 vehicle semi-active suspension using the MR damper, and the influence of frictional force on the performance evaluation indexes of passive and semi-active suspensions is investigated. The simulation results indicate that the influence of frictional force on semi-active suspension is higher than that of passive suspension, and reducing the frictional force of the MR damper is of great significance to improve the performance of the semi-active suspension.

Keywords

MR damper, low friction, semi-active suspension, cavitation effect

Date received: 31 May 2023; accepted: 29 August 2023

Introduction

The main function of automobile suspension is to alleviate the impact load transmitted from the uneven road surface to the body, attenuate the vibration, and improve passenger comfort and vehicle dynamic performance.¹ The springs and dampers of the suspension play the roles of buffering and damping, respectively. Generally, automobile suspension is divided into traditional passive suspension, semi-active suspension, and active suspension.² The stiffness and damping of the traditional suspension are not adjustable, making it difficult to meet the functional and performance requirements of the suspension when the vehicles are driving under different conditions.³ The active suspension can adjust the stiffness and damping of the suspension promptly according to the movement of the vehicle and the road surface conditions. Thus, the active suspension

¹Anhui Key Laboratory of Digit Design and Manufacture, Hefei University of Technology, Hefei, People's Republic of China

²Key Laboratory for Automated Vehicle Safety Technology of Anhui Province, Hefei University of Technology, Hefei, People's Republic of China

³Engineering Research Center for Intelligent Transportation and Cooperative Vehicle-Infrastructure of Anhui Province, Hefei University of Technology, Hefei, People's Republic of China

⁴Laboratory for Adaptive Structures and Intelligent Systems, Department of Vehicle Engineering, Hefei University of Technology, Hefei, People's Republic of China

Corresponding author:

Xianxu 'Frank' Bai, Laboratory for Adaptive Structures and Intelligent Systems, Department of Vehicle Engineering, Hefei University of Technology, RM. 423, Gewu Building, Tunxilu, 193#, Hefei, Anhui 230009, People's Republic of China.
 Email: bai@hfut.edu.cn

is always in the optimal vibration reduction state, with fast response and excellent performance. However, the problems of high energy consumption, complex structure, and high failure rate hinder its large-scale application.^{4,5} The semi-active suspension does not change the stiffness of the suspension, but only changes the damping. It has features of simple structure, low energy consumption, and high performance comparable to active suspension,^{6,7} making it have a good application prospect. At present, the dampers of commercial semi-active suspensions mainly include continuous damping control dampers and magnetorheological (MR) dampers. Among them, the MR damper is an active variable damping device that utilizes the rheological effect of the internal MR fluid under the action of a magnetic field to change the damping properties of the MR damper.⁸ The damping can be continuously adjusted by adjusting the magnitude of the loading current. The MR damper has the advantages of fast response, small size, low energy consumption, and easy control,^{9–13} which has attracted wide attention in the fields of automobile,^{14,15} bridge,¹⁶ military,¹⁷ and so on.

The MR dampers can markedly improve the handling and comfort of vehicles. It had been proved that the root mean square (RMS) value of the vertical acceleration of the vehicle body can be significantly reduced by a self-sensing automotive MR damper.¹⁸ In order to improve the performance of MR dampers, scholars are committed to improving the semi-active vibration control methods and optimizing the structure of MR dampers. Ma et al.¹⁹ optimized a fuzzy skyhook control method to simultaneously reduce the amplitude of vertical acceleration, suspension deflection, and dynamic tire load. Dong et al.²⁰ designed a new type of parallel gap MR damper with a check valve structure, which greatly reduces the installation space and improves the vibration damping performance. Jiang et al.²¹ designed an MR damper with internal channels in the piston and optimized the structure. The magnetic circuit was integrated into the piston assembly, so that the components of the MR damper are easy to modularize, light in weight, and good in electromagnetic compatibility. It is verified by experiments that the optimized MR damper has a reasonable magnetic circuit and excellent performance.

The most important factors affecting the vibration control effect of MR semi-active suspension include the response time of MR damper²² and the dynamic range of damping force.¹² In order to enhance the suspension performance, the response time of the MR damper should be fast enough.²³ Strecker et al.²⁴ identified three main sources of extending response time as MR fluid, electronic circuits (especially coil inductance), and magnetic circuits (eddy currents). They designed a current controller to minimize the response time of the circuit using a pulse width modulation technique. Yoon et al.²⁵ designed an MR damper with a very small eddy current distribution using soft magnetic composite materials with high resistivity, and verified through experiments

that reducing the eddy current around the magnetic field area can reduce the response time of MR damper.

The MR damper should also have a larger dynamic range of damping force to achieve better vibration isolation performance. The damping force of MR damper consists of controllable damping force and uncontrollable damping force. The dynamic range of the damping force can be expanded by increasing the controllable damping force or decreasing the uncontrollable damping force. In previous studies, to the authors' knowledge, researchers typically increased the dynamic range of damping force by increasing the controllable damping force. In order to obtain better damping capacity, researchers have conducted a lot of research. Yan and Dong²⁶ designed a MR damper with double-annular damping gap. Compared with conventional MR dampers, the MR dampers have larger damping force and dynamic range. Hu et al.²⁷ proposed a multi-objective optimization design method based on a multi-physics field coupling model. Experimental results showed that the damping force and dynamic range of the optimized MR damper were increased by 21.9% and 11.9%, respectively, compared to the original MR damper. Liu et al.²⁸ proposed an external multi-pole MR damper, which adopted the design of multiple electromagnetic poles integrated into the cylinder to obtain a larger damping force control range. Gaoyu et al.²⁹ designed an MR damper with multiple grooves, that is multiple small annular flow gaps, on the piston. A simulation comparison was conducted between MR dampers with and without multiple grooves. The results showed that the MR damper with multiple grooves has larger damping force and controllable force range. Liu et al.³⁰ optimized the shape of MR damper piston based on parameter curves, and the controllable force range of the MR damper with the optimized piston is larger than that of the ordinary piston.

The uncontrollable damping force consists of viscous force and frictional force.³¹ The viscous force depends on the channel structure of the MR damper and the dynamic viscosity of the MR fluid.³² While the frictional force is mainly caused by mechanical seals, and its magnitude is related to the MR damper inflation pressure. When the MR damper is compressed at a low speed with a given high excitation current, it will encounter difficulties in the flow of the MR fluid at both ends of the annular damping channel, resulting in a decrease in MR fluid pressure. When the static pressure is lower than the steam pressure, some MR fluid will transform from liquid state to gas state, resulting in damping force distortion, which is called "cavitation effect." To avoid the cavitation effect, MR dampers need to be filled with high-pressure compensation gas,³³ which leads to excessive-high frictional force in the MR dampers and affects the vehicle ride comfort. To further improve the performance of MR damper, one of the feasible methods is to reduce the frictional force of the damper. However, relevant research is rarely reported.

Aiming at the problem of high frictional force in MR dampers, a monotube MR damper with low friction and high performance is proposed in this study. The pressure of the compensation gas of the damper is reduced through the structural design. Besides, the influence of frictional force on the vibration isolation performance of electronically controlled suspension is studied through system performance simulation. The main contributions of this work are as follows: (1) a monotube MR damper with low-friction is proposed, in which a bottom valve structure is used to reduce the inflation pressure, thereby reducing the frictional force; (2) the parameters of the key structure of the MR piston are optimized, and the valve system of the damper is matched to make the proposed MR damper only need to be filled with low-pressure compensation gas to ensure the normal flow of the MR fluid without cavitation effect; and (3) in order to study the influence of low-friction MR damper on improving suspension performance, the influence of damper frictional force on suspension system is evaluated based on the sprung mass acceleration RMS and dynamic tire load RMS.

Structure and principle of low-friction MR damper

In order to solve the problem of damping force distortion caused by cavitation effect, the conventional MR damper needs to increase the compensation gas pressure in the gas storage chamber, which is the main reason for the high frictional force and low life of the sealing structure of MR damper. Reducing the compensation gas pressure in the gas storage chamber of the MR damper can effectively reduce the frictional force of the damper. In this study, a low-friction MR damper was designed by reducing the maximum pressure of the MR piston head in the compression stroke and introducing a bottom valve structure with compression valve to compensate for the reduced pressure of the MR piston head. This MR damper only needs to be filled with low-pressure compensation gas, and the MR fluid can flow normally at both ends of the annular damping channel. Thus, it achieved the purpose of outputting the same compression damping force as conventional MR damper without cavitation effect.

Structure and working principle

As shown in Figure 1(a), the proposed low-friction MR damper is mainly composed of an MR piston that outputs controllable damping force, a bottom valve that outputs uncontrollable damping force, a floating piston that compensates the volume of MR fluid, a top guide-seal component, and a cylinder. The structure of the MR piston that outputs controllable damping force is shown in Figure 1(b). The piston rod, iron core, and piston sleeve are concentrically arranged through the upper and lower limit end caps of the piston and are

fixedly connected by crimping. The annular damping channel formed by the iron core and the piston sleeve is the area where the MR piston outputs controllable damping force. The axial movement, that is, compression or rebound, of the piston drives the MR fluid in the cylinder to form pressure at both ends of the annular damping channel to generate damping force. The electromagnetic coil is connected to the external controller through the axial through-hole of the piston rod. By adjusting the excitation current acting on the electromagnetic coil, different intensities of magnetic fields are generated in the annular damping channel, and the yield stress of the MR fluid in the channel is changed accordingly. Thus, the control of outputting different damping forces is realized. The outer wall of the coil group and the bottom of the iron core are coated with LORD310 epoxy resin adhesive, which can withstand an extreme temperature of up to 204°C, avoiding the problem of sealing degradation caused by the rapid temperature rise of the MR damper under harsh working conditions.

The top guide-seal component is one of the main sources of friction for dampers. As shown in Figure 1(c), the top guide-seal component consists of a Y-shaped sealing ring for piston rod sealing, a guide copper sleeve, a dust-proof oil seal, and a top support with an O-ring on outer wall for static sealing of cylinder. The customized Y-shaped sealing ring is made of fluorine rubber, with a working temperature range of -30°C to 200°C, a working speed above 1.5 m/s, and a withstand pressure difference up to 31.5 MPa. It has strong sealing and high temperature resistance and can fully meet the performance requirements of MR dampers. The two annular grooves of the floating piston are equipped with O-rings for dynamic sealing, which isolate the MR fluid in the liquid storage chamber from the high-pressure nitrogen in the gas storage chamber.

In general, the damper of passenger car needs to output asymmetric mechanical characteristics. Specifically, the damper needs to output a small damping force for buffering in the compression stroke, while output a large damping force to absorb the energy stored in the suspension spring for vibration isolation in the rebound stroke. Fully considering the damping force requirements in each stroke, the low-friction MR damper structure proposed in this study not only includes an annular damping channel for the MR piston to generate controllable damping force, but also adds a compression valve, a flow valve, and a compensation valve to achieve asymmetric mechanical characteristics. The flow valve and the compensation valve are one-way valves, which can reach the valve opening state with a very low pressure and are installed at the MR piston and the bottom valve, respectively. The compression valve is an unloading valve installed at the bottom valve, which can only be opened when the pressure increases to a certain threshold.

Figure 2 shows how each valve system works during the rebound and compression strokes of the low-

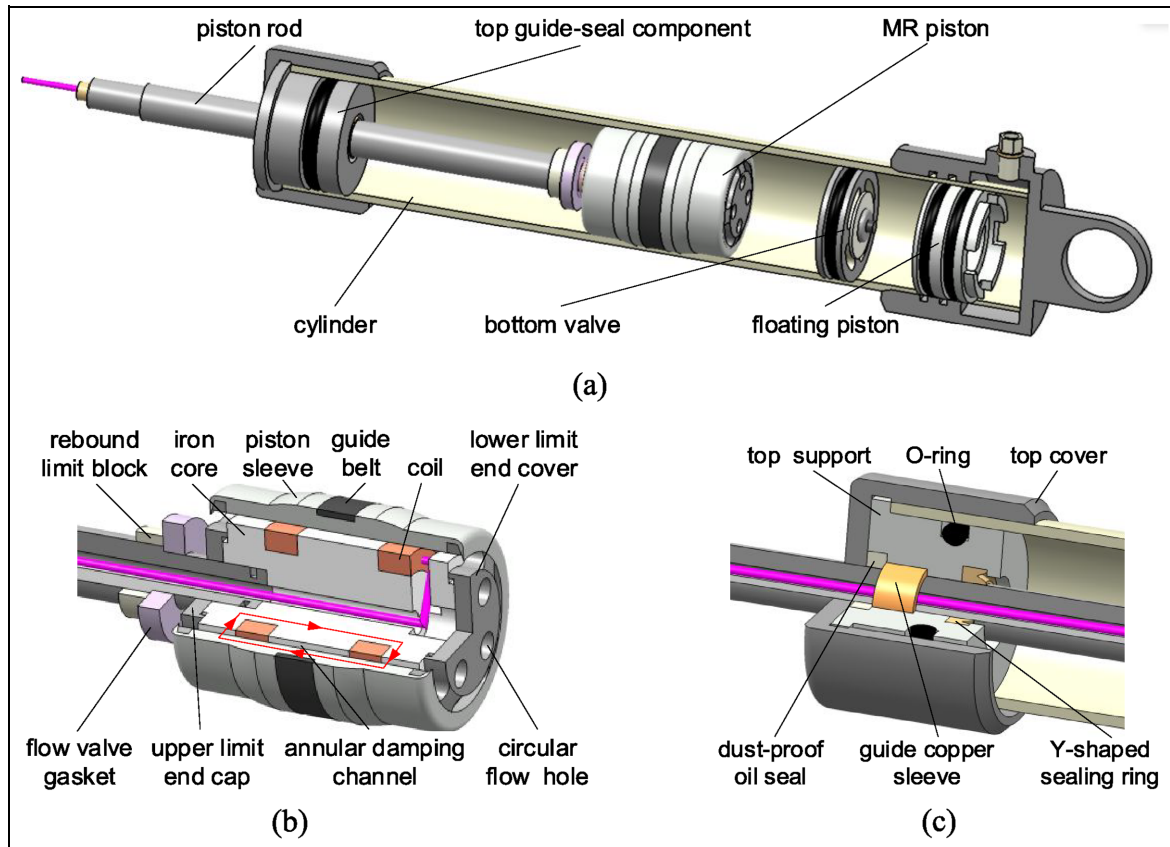


Figure 1. Low-friction MR damper structure: (a) assembly drawing, (b) MR piston structure, and (c) top guide-seal component structure.

friction MR damper. As shown in Figure 2(a), when the low-friction MR damper is in the rebound stroke, the pressure in the rebound chamber rises, the flow valve and compression valve are closed, and the compensation valve is opened. The fluid of the rebound chamber flows into the compression chamber through the annular damping channel of the MR piston, and the pressure is generated between the ends of the annular damping channel of the MR piston to output the damping force. The piston rod occupies a certain volume of the rebound chamber of the damper, and the fluid of the rebound chamber alone cannot fill the compression chamber. Therefore, the compression chamber of the damper produces a certain degree of vacuum. Driven by the compensation gas with a certain initial pressure, the MR fluid in the liquid storage chamber pushes the compensating valve open and flows into the damper compression chamber, compensating for the volume of oil discharged by the moving piston rod.

As shown in Figure 2(b), when the low-friction MR damper is in the compression stroke, the volume of the compression chamber reduces, and the fluid pressure increases. Therefore, the flow valve opens, and part of the fluid in the compression chamber enters the rebound chamber through the flow valve and the annular damping channel. Because the piston rod in the rebound chamber occupies a part of the fluid volume,

part of the MR fluid flows into the liquid storage chamber through the hole in the compression valve. When the compression speed is fast, the compression valve opens for unloading. During this period, the compression damping force comes from the pressure generated by the bottom valve, the annular damping channel on the MR piston, and the flow valve round hole.

Modeling of mechanical properties

Based on the polar plate flow model of the fluid, the mechanical model of the low-friction MR damper is established. When the low-friction MR damper is in the rebound stroke, the damping force comes from the annular damping channel on the MR piston. While in the compression stroke, the damping force is jointly generated by the annular damping channel, the flow valve round hole and the bottom valve of the MR piston. The damping force in the rebound stroke, F_r , and the damping force in the compression stroke, F_c , can be expressed as:

$$\begin{cases} F_r = F_{r_ctrl} + F_{r_unctrl} \\ F_c = F_{c_ctrl} + F_{c_unctrl} \end{cases} \quad (1)$$

where, F_{r_ctrl} is the controllable damping force in the rebound stroke; F_{r_unctrl} is the uncontrollable damping

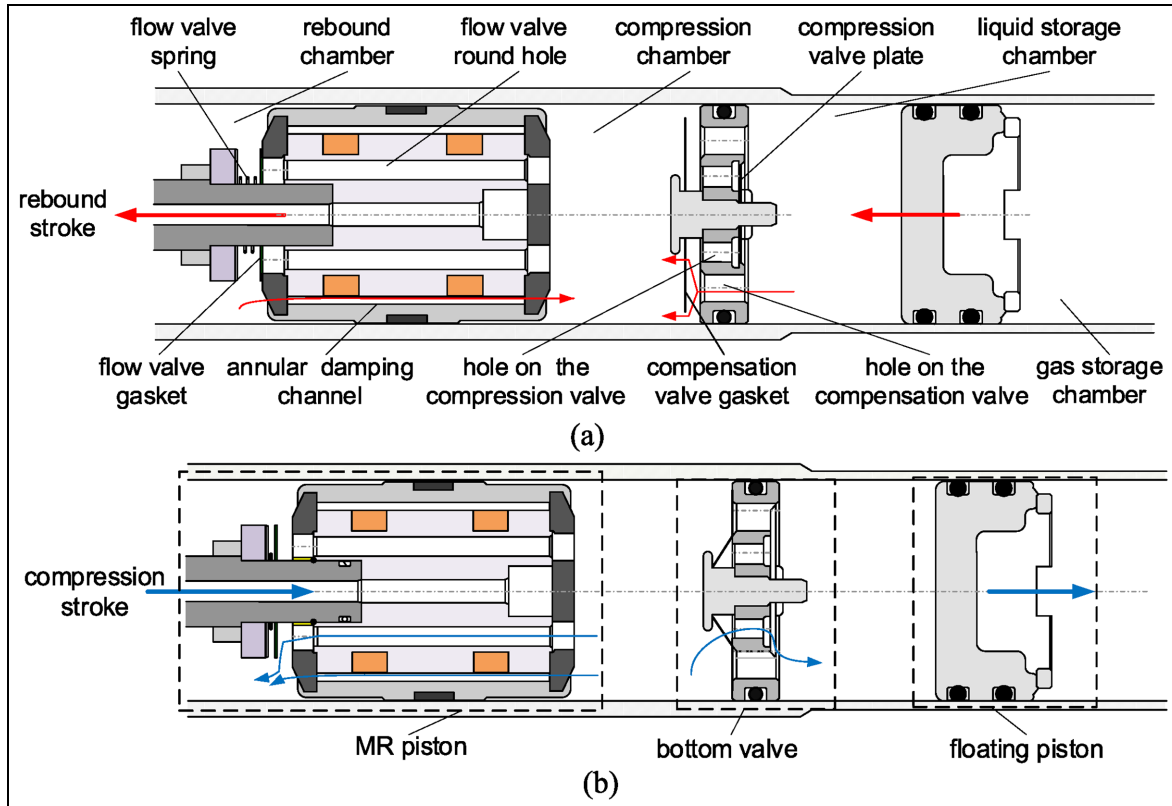


Figure 2. Working principle of each valve system in different strokes: (a) rebound stroke and (b) compression stroke.

force in the rebound stroke; F_{c_ctrl} is the controllable damping force in the compression stroke; and F_{c_unctrl} is the uncontrollable damping force in the compression stroke.

Modeling of controllable damping force. The controllable damping force in the rebound and compression strokes can be expressed as:

$$\begin{cases} F_{r_ctrl} = \frac{cl_a \tau_y A_\eta}{h} \\ F_{c_ctrl} = \Delta p_{12\tau} A_\eta \end{cases} \quad (2)$$

where, l_a is the effective length of the magnetic field; h is the gap of the damping channel; τ_y is the yield stress of the MR fluid; $\Delta p_{12\tau}$ is the partial pressure caused by the magnetic field, which is part of the pressure difference between the fluid pressure p_1 in the rebound chamber and the fluid pressure p_2 in the compression chamber; A_η is the effective area of the piston; and c is a fixed coefficient, which can be expressed as³⁴:

$$c = \begin{cases} 2, & \Delta p_{12\eta} / \Delta p_{12\tau} < 1 \\ 3, & \Delta p_{12\eta} / \Delta p_{12\tau} > 100 \end{cases} \quad (3)$$

where, $\Delta p_{12\eta}$ is the partial pressure caused by the viscous resistance of MR fluid, which is the other part of the pressure difference between the fluid pressure p_1 in the rebound chamber and the fluid pressure p_2 in the compression chamber.

The yield stress τ_y of MR fluid is determined by the intensity of the magnetic field B_0 , which is determined by the intensity of the magnetic induction. The higher the magnetic field intensity, the stronger the flux linkage formed by the ferromagnetic particles in the MR fluid between the two plates along the direction of the magnetic induction line, and the greater the yield stress of the MR fluid. The relationship between yield stress and magnetic induction intensity of MR fluid measured experimentally is shown in Figure A1. Based on Figure A1, the yield stress of MR fluid can be obtained as equation (4) by polynomial fitting:

$$\tau_y = \alpha_0 + \alpha_1 B_0 + \alpha_2 B_0^2 + \alpha_3 B_0^3 + \alpha_4 B_0^4 \quad (4)$$

where, B_0 is the magnetic induction intensity, which is related to the current flowing into the excitation coil; α_0 , α_1 , α_2 , α_3 , and α_4 are the polynomial fitting coefficients of τ_y , which are listed in Table A1.

When the MR damper is in the compression stroke, the flow valve of the MR piston is opened, and part of the MR fluid flows parallel into the rebound chamber from the compression chamber through the annular damping channel of the MR piston and four flow valve round holes. In the compression stroke, the partial pressure caused by the magnetic field $\Delta p_{12\tau}$ can be expressed as:

$$\Delta p_{12\tau} = \frac{32cl_a D_0 h^2}{32D_0 h^3 + 3N d^4} \tau_y \quad (5)$$

where, D_0 is the equivalent diameter of the annular damping channel; d is the diameter of the flow valve round hole; N is the number of the flow valve round holes, which is 4 for the proposed low-friction MR damper piston. Equation (5) expresses the relationship between the partial pressure caused by the magnetic field $\Delta p_{12\tau}$ and the yield stress τ_y of the MR fluid when the low-friction MR damper is in the compression stroke. It can be obtained from the relationship between the flow rate of the fluid flowing into the rebound chamber of the damper, q_2 , the flow rate of the fluid in the annular damping channel, q_e , and the total flow rate of the fluid flowing through the four flow valve round holes, q_f . The flow rate of the fluid flowing into the rebound chamber of the damper, q_2 , is the sum of the flow rate of the fluid flowing through the annular damping channel, q_e , and the total flow rate of the fluid flowing through the four flow valve round holes, q_f , which can be expressed as:

$$q_2 = q_e + q_f = A_\eta v \quad (6)$$

where, v is the relative velocity of the damper.

According to the pressure relationship equation of the annular damping channel derived by Phillips³⁴ based on the flat plate model, the flow rate of the fluid flowing through the annular damping channel can be deduced as:

$$q_e = \frac{\pi D_0 h^3}{12\eta l} \left(\Delta p_{12} - \frac{c l_a \tau_y}{h} \right) \quad (7)$$

where, η is the dynamic viscosity of the MR fluid piston; $\Delta p_{12} = p_1 - p_2$.

The magnetic field inside the flow valve round hole can be ignored, so the flow rate here is only affected by the viscosity effect of the MR fluid. Since the ratio of the effective length l of the piston to the diameter d of the hole being no less than 4, it can be regarded as the flow in slender hole, which is a laminar flow state. Thus, the flow rate of the fluid flowing in the four flow valve round holes can be derived as:

$$q_f = \frac{N\pi\Delta p_{12}d^4}{128\eta l} \quad (8)$$

According to equations (6)–(8), the expression of Δp_{12} can be obtained as:

$$\Delta p_{12} = \frac{384\eta A_\eta l}{32\pi D_0 h^3 + 3N\pi d^4} v + \frac{32c l_a D_0 h^2}{32D_0 h^3 + 3Nd^4} \tau_y \quad (9)$$

The first term on the right side of equation (9) is the partial pressure $\Delta p_{12\eta}$, and the second term is the partial pressure $\Delta p_{12\tau}$.

Modeling of uncontrollable damping force. The uncontrollable damping force in the rebound and compression strokes can be expressed as:

$$\begin{cases} F_{r_unctrl} = \frac{12\eta l A_\eta^2}{\pi D_0 h^3} v \\ F_{c_unctrl} = \Delta p_{12\eta} A_\eta + (p_3 - p_0) A_r + \Delta p_{23} A_r + f \end{cases} \quad (10)$$

where, p_3 is the fluid pressure in the liquid storage chamber; p_0 is the atmospheric pressure; A_r is the cross-sectional area of the piston rod; $\Delta p_{23} = p_2 - p_3$; f is the frictional force of the damper, which is determined by the structural design and the inflation pressure; $\Delta p_{12\eta}$ is the first term on the right side of equation (9) is the partial pressure, which is rewritten as following.

$$\Delta p_{12\eta} = \frac{384\eta A_\eta l}{32\pi D_0 h^3 + 3N\pi d^4} v \quad (11)$$

Equation (11) expresses the relationship between the partial pressure $\Delta p_{12\eta}$ at the MR piston caused by the viscous resistance of the MR fluid and the relative velocity v when the low-friction MR damper is in the compression stroke.

Since this work mainly studies the frictional force generated by the top guide-seal components, it is assumed that the pressure in the liquid storage chamber is the same as the pressure in the gas storage chamber in the simplified model. So $p_3 - p_0$ can be expressed as:

$$p_3 - p_0 = p_g = p_{g0} \left(\frac{V_{g0}}{V_{g0} + A_\eta x_p} \right)^n \quad (12)$$

where, p_g is the pressure in the gas storage chamber; p_{g0} is the initial pressure of the gas storage chamber when the damper is at the rebound limit position; V_{g0} is the volume of the gas storage chamber when the damper is at the rebound limit position; x_p is the displacement of the piston relative to the cylinder at a certain moment; n is the gas adiabatic coefficient.

During the compression stroke, part of the MR fluid in the compression chamber flows into the liquid storage chamber through the compression valve on the bottom valve, and a pressure difference of Δp_{23} is generated between the two ends of the bottom valve. Figure 3 shows the working principle of the bottom valve. When the pressure of the bottom valve is low, the valve opening point is not reached, and only the holes of the compression valve and the throttling slots of the slotted valve plate are connected in series to generate a pressure difference. When the relative velocity v of the damper exceeds the critical velocity v_{cr} for compression valve opening, the fluid pushes open the compression valve plate and flows simultaneously through the throttling slots of the slotted valve plate and the annular gap formed by the deformation of the stacked valve plate under the action of fluid pressure.

The pressure difference Δp_{23} between the two ends of the bottom valve when the compression valve is closed ($v \leq v_{cr}$) and opened ($v > v_{cr}$) can be expressed as:

$$\Delta p_{23} = \begin{cases} \frac{128\eta l_b A_r}{N_b \pi d_b^4} v + \frac{\rho A_r^2}{2C_d^2 N_c^2 \lambda_k^2 h_0^2} v^2, & v \leq v_{cr} \\ \frac{128\eta l_b A_r}{N_b \pi d_b^4} v + \frac{T_K + \sqrt{T_K^2 - 36\eta^2 (ln(a/b))^2 \pi^2 f_0^6 A_r^2 \rho^2 v^2}}{\pi^2 f_0^6 \rho}, & v > v_{cr} \end{cases} \quad (13)$$

where, N_b is the number of the holes on the compression valve; l_b is the effective length of the hole on the compression valve; d_b is the diameter of the hole on the compression valve; C_d is an coefficient which is usually between 0.60 and 0.61; ρ is the fluid density; N_c is the number of rectangular normally open throttling slots; λ_k is the slot width; h_0 is the thickness of the slotted valve plate; a is the outer radius of the valve plate; b is the inner support radius of the valve plate; f_0 is the bending deformation of each stacked valve plate; $T_K = 6\pi A_r v \rho f_0^3 \eta \ln(a/b) + 36\eta^2 (\ln(a/b))^2 C_d^2 N_c^2 \lambda_k^2 h_0^2$.

Equation (13) describes the relationship between the pressure difference Δp_{23} between the two ends of the bottom valve and the relative velocity v when the low-friction MR damper is in the compression stroke, with the compression valve closed and opened. The pressure difference Δp_{23} between the two ends of the bottom valve is the sum of the pressure Δp_a generated by the hole on the compression valve and the pressure Δp_b generated by the slotted valve plate.

$$\Delta p_{23} = \Delta p_a + \Delta p_b \quad (14)$$

The pressure difference between the two ends of the holes on the compression valve, which are four slender holes, can be derived as:

$$\Delta p_a = \frac{128\eta l_b A_r}{N_b \pi d_b^4} v \quad (15)$$

In general, the valve plates are extremely thin, and their throttling process can be regarded as a thin-wall-small-hole throttle form. Therefore, the relationship between the flow rate of the fluid flowing through the throttling slots of the slotted valve plate and the pressure Δp_b can be expressed as:

$$q_b = C_d N_c \lambda_k h_0 \sqrt{\frac{2\Delta p_b}{\rho}} \quad (16)$$

When $v \leq v_{cr}$, the compression valve is closed, the flow rate q_a of MR fluid passing through the holes of the compression valve is equal to the flow rate q_b through the throttling slots of the slotted valve plate, as expressed in equation (17). And the volume of this part of MR fluid is equal to the volume of fluid discharged by the piston rod.

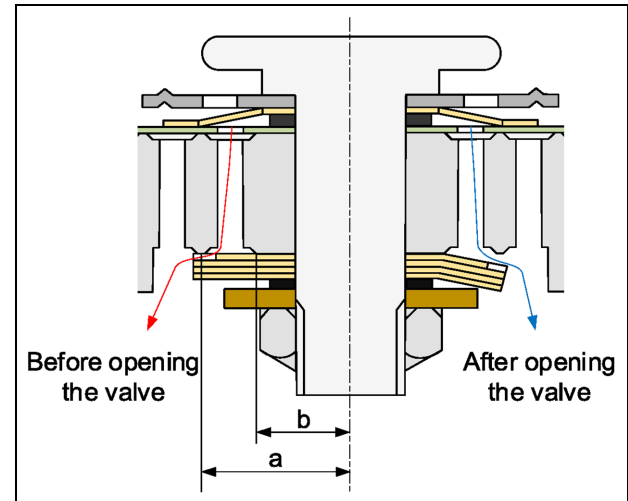


Figure 3. Schematic diagram of the working principle of the compression valve.

$$q_a = q_b = A_r v \quad (17)$$

According to equations (14)–(17), the pressure difference Δp_{23} when the valve is closed, shown as the first term of equation (13), can be obtained.

When $v > v_{cr}$, the pressure acting on the compression valve plate reaches the pre-tightening force of the elastic slotted valve plate. At this time, the MR fluid pushes the compression valve open, forming an annular throttling gap. The flow rate q_c through the annular throttling gap can be expressed as:

$$q_c = \frac{\pi f_0^3 \Delta p_c}{6\eta \ln(a/b)} \quad (18)$$

where, Δp_c is the pressure generated by the stacked valve plate. According to *Mark's Calculations for Machine Design*,³⁵ the deformation of the stacked valve plate at the outer radius of the valve is:

$$f_0 = C_6 \frac{\Delta p_c a^4}{E \delta^3} \quad (19)$$

where, E is the elastic modulus of the stacked valve plate; δ is the equivalent radius of the stacked valve plate. C_6 is the maximum deflection coefficient, which is determined by the radius ratio a/b , and can be obtained by quartic polynomial fitting of the data given in Brown.³⁵

$$C_6 = \beta_0 + \beta_1 \frac{a}{b} + \beta_2 \left(\frac{a}{b}\right)^2 + \beta_3 \left(\frac{a}{b}\right)^3 + \beta_4 \left(\frac{a}{b}\right)^4 \quad (20)$$

where, $\beta_0, \beta_1, \beta_2, \beta_3$, and β_4 are the polynomial fitting coefficients of C_6 , which are listed in Table A1.

At this time, the total flow rate q_a at the bottom valve is:

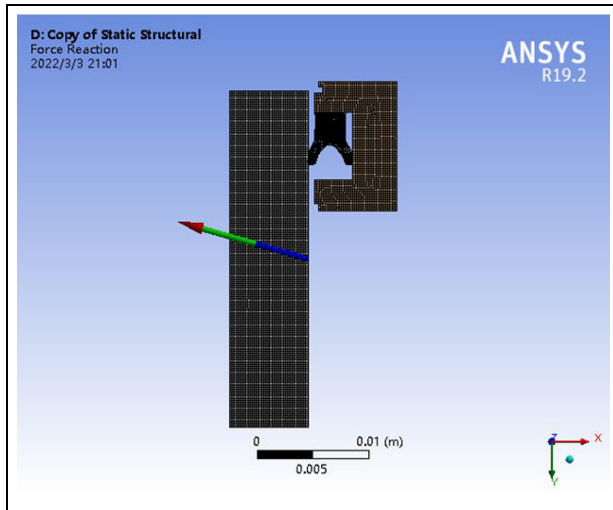


Figure 4. Simulation of Y-shaped sealing ring friction.

$$q_a = q_b + q_c = A_r v \quad (21)$$

$$\Delta p_b = \Delta p_c \quad (22)$$

According to equations (14)–(16) and equations (18)–(22), the pressure difference Δp_{23} when the valve is open, shown as the second term of equation (13), can be obtained.

Analysis of the influence of gas pressure on the frictional force of the damper. There are two main types of sources of frictional force in dampers: one is independent of the gas pressure, while the other is related to the gas pressure. The sources independent of the gas pressure include lateral force, dust-proof oil seal with large assembly interference, and guiding components affected by assembly accuracy such as piston rod, guiding copper sleeve, and piston guiding belt. While the sources related to the gas pressure are the sealing components affected by gas pressure such as piston rod sealing ring and O-ring. According to QC/T 545-1999 *Bench test methods for Telescopic Shock Absorbers Used on Car*, the frictional force independent of gas pressure is measured to be 14 N at an excitation speed of less than 5 mm/s. The elastic sealing components of the frictional force related to the gas pressure are mainly the Y-shaped sealing ring between the piston rod and the cylinder and the O-ring between the floating piston and the cylinder. Among them, the main contribution of the frictional force related to the gas pressure comes from the Y-shaped sealing ring. Therefore, this study mainly analyzes the influence of gas pressure and other factors on the frictional force of the Y-shaped sealing ring. The Y-shaped sealing ring is fixed in the top guide-seal components, with the notch facing the side with fluid. When the damper is in the rebound and compression stroke, the deformation of the Y-shaped sealing ring is different, as well as the frictional force.

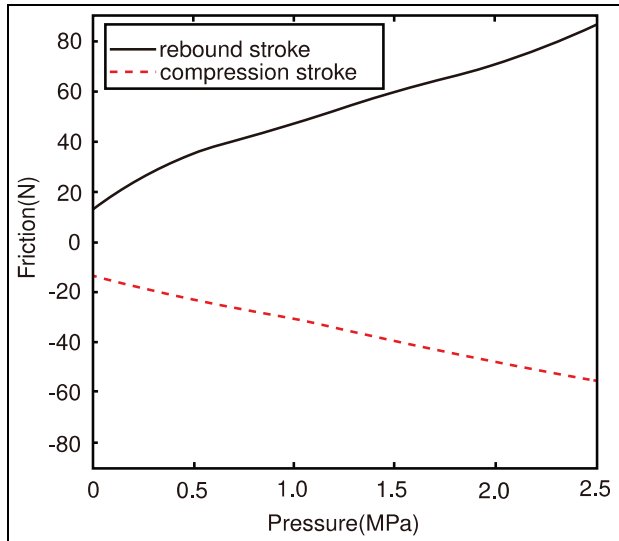


Figure 5. The frictional force of Y-ring under different pressures and strokes.

To investigate the influence of gas pressure on the frictional force of low-friction MR damper, the influence of gas pressure on the frictional force of Y-shaped sealing ring is studied, and a 2D finite element model is established as shown in Figure 4. The Y-shaped sealing ring is made of fluorine rubber and the act on the lip of the Y-shaped sealing ring is even. The piston rod is made of 20# steel with chrome-plated surface. The friction factor between the sealing ring and the piston rod is 0.3.

Figure 5 shows the stable frictional force curves corresponding to the pressure ranging from 0 to 2.5 MPa during the rebound and compression strokes. The rebound velocity is defined as positive, while the compression velocity is negative. On the one hand, both the frictional forces in the compression and rebound strokes increase with the increase of pressure, and the change rate of the frictional force in the rebound stroke with pressure is greater than that in the compression stroke. It indicates that the rebound stroke is more affected by the pressure. On the other hand, the magnitude of the frictional force is related to the direction of motion, that is, the stable frictional force during the rebound stroke is greater than that during the compression stroke. It is thus clear that the controllable characteristics of the rebound stroke of low-friction MR damper are more affected by friction than that of the compression stroke.

Figure 6 shows the friction deformation process of the Y-shaped sealing ring in the rebound stroke. Figure 6(a) is the static state without applying any pressure, which shows that the Y-shaped sealing ring has no deformation. Figure 6(b) shows that the lip of the sealing ring undergoes approximately uniform deformation under a certain pressure. The sealing ring undergoes axial compression deformation, and the sealing lips on the left and right sides expand evenly toward each end.

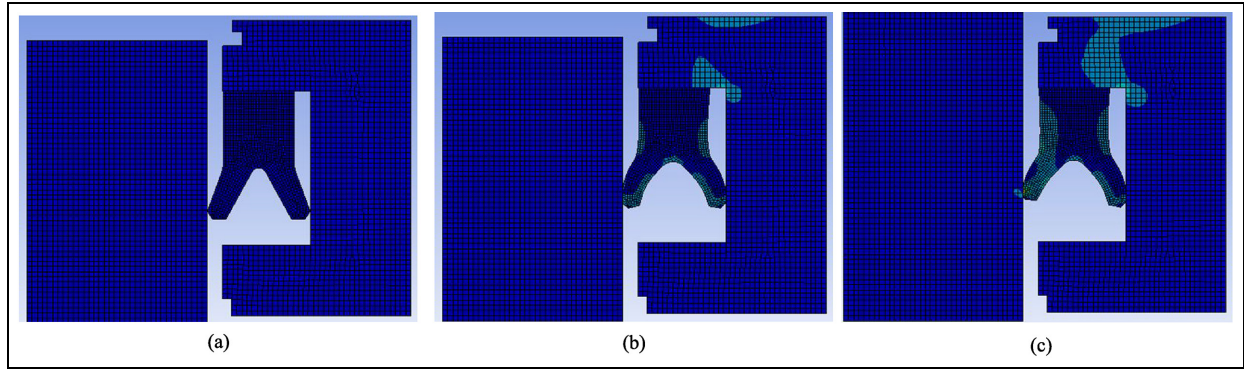


Figure 6. Deformation process of the Y-shaped sealing ring: (a) the Y-shaped sealing ring does not deform when no pressure is applied, (b) deformation of the Y-shaped sealing ring during the compression stroke when a certain pressure is applied, and (c) deformation of the Y-shaped sealing ring during the rebound stroke when a certain pressure is applied.

Figure 6(c) shows the deformation of the Y-shaped sealing ring during the rebound stroke. Under the action of dynamic frictional force, the left sealing lip undergoes secondary compression deformation, resulting in an increase in contact stress. Therefore, the frictional force during the rebound stroke is higher.

Optimization of low-friction MR damper parameters

The proposed low-friction MR damper is a complex system composed of an electronically controlled MR piston and pressure-generating components such as passive valve holes and valve plates. On the one hand, in order to make its structure more reasonable, have a larger controllable damping force range, and have fewer coil turns, it is necessary to optimize the structural parameters of the MR piston. On the other hand, in order to avoid the cavitation effect of the low-friction MR damper under the condition of low-pressure compensation gas, it is necessary to match the pressures generated by the MR piston and the bottom valve.

Optimization of MR piston parameters

In order to make the magnetic field distribution reasonable, improve the dynamic range of damping force of the low-friction MR damper, and reduce the response time, the piston structure with dual-coil is adopted. The low-friction MR damper piston has many structural parameters. To seek a set of parameters that output the ideal range of damping force, the structural design of the MR piston is transformed into a multi-objective optimization problem. In this study, the objective function is to maximize the controllable damping force of the MR piston in the compression stroke, which is determined by $\Delta p_{12\tau}$, and reduce the number of turns of the excitation coil N_{coil} to improve the response speed of the MR damper and reduce the process cost. The weighted sum method is used to transform the problem into the following form:

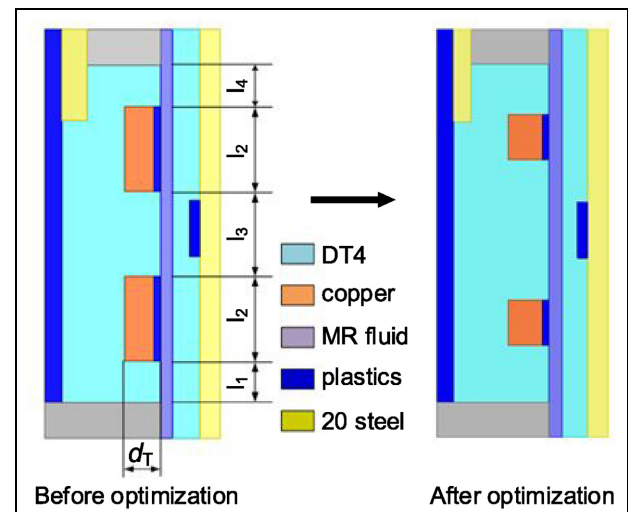


Figure 7. Comparison of the cross-section of MR piston before and after optimization.

$$\min Q(\Delta p_{12\tau}, N_{\text{coil}}) = w_1 \frac{p_k - \Delta p_{12\tau,\text{opt}}}{p_k - \Delta p_{12\tau}} + w_2 \frac{N_{\text{coil,opt}}}{N_{\text{coil}}} \quad (23)$$

where, w_1 is the weight coefficient of the pressure generated by the magnetic field; w_2 is the weight coefficient of the number of the coil turns; $\Delta p_{12\tau,\text{opt}}$ is the pressure generated by the optimized magnetic field; p_k is a fixed parameter introduced to unify the maximization of magnetic field pressure into the minimization problem; and $N_{\text{coil,opt}}$ is the number of the optimized coil turns. The relationship between the number of the coil turns and the cross-sectional area $S(\text{m}^2)$ of the coil group has been determined by experiments as:

$$N_{\text{coil}} = \frac{S}{2.8717 \times 10^{-7}} \quad (24)$$

As shown in Figure 7, the length of the magnetic field action area of each segment of the MR piston is

Table 1. MR piston optimization results.

Parameter	Before optimization	After optimization
l_1 (mm)	6	8
l_2 (mm)	12	6.5
l_3 (mm)	12	20
l_4 (mm)	6	7
d_T (mm)	5	6
N_{coil} (turns)	376	250
F_{r_ctrl} (N)	875	851
Q	1	0.799

l_1 , l_2 , l_3 , and l_4 . Among them, l_2 is the length of the excitation coil slot. d_T is the design variable of the coil groove depth. Besides, the total length of the piston, the width of the annular damping channel, and the radial position are all constants. In this study, ignoring the secondary factors such as rounded corners, the magnetic field simulation model of the proportional half section MR piston is established. The iron core and piston sleeve are made of pure electrical iron DT4, the upper and lower limit end caps of the piston are made of 7075 aluminum, the piston rod is made of 20# steel, and the sealing layer and guiding belt are made of polytetrafluoroethylene plastics. The finite element optimization model for the electromagnetic field of the MR piston is established using ANSYS/APDL. The cross-section of the MR piston before and after optimization is shown in Figure 7.

Table 1 lists the dimensions of the key structural parameters of the MR piston before and after optimization. The data in Table 1 shows that the objective function Q has been reduced from 1 to 0.765, which reflects that the total cost of the optimized structure is reduced; The axial length of the coil slot has been reduced from 12 to 6.5 mm, saving a large axial space for the effective area of the magnetic field. In the rebound stroke, the controllable damping force range of the proposed low-friction MR damper only slightly decreased from 875 to 851 N, a decrease of 2.7%. While the number of coil turns has been reduced from 376 to 250, a decrease of up to 33.5%. Therefore, on the basis of ensuring the controllable force range, the manufacturing cost is greatly reduced, and the response speed is also improved.

The static magnetic field simulation of the optimized MR piston is carried out using ANSYS finite element software. The distribution of the magnetic induction lines of the optimized low-friction MR damper piston at the excitation current of 2.0 A is shown in Figure 8(a). Most of the magnetic induction lines inside the piston structure pass through the annular damping channel along the iron core and form a loop with the piston sleeve. The magnetic induction intensity cloud diagram is shown in Figure 8(b), where the peak magnetic induction intensity is reached at the piston sleeve of the MR piston. The magnetic induction intensity generated by the electromagnetic coil has a significant correlation

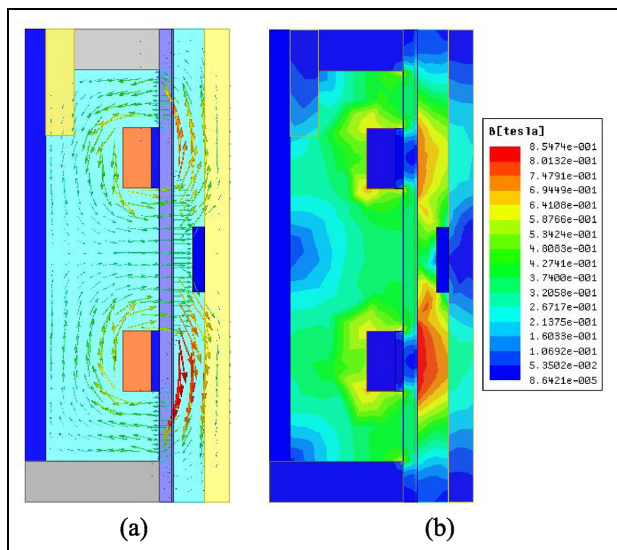


Figure 8. Static magnetic field simulation results when the excitation current is 2A: (a) distribution of magnetic induction lines and (b) distribution of magnetic induction intensity.

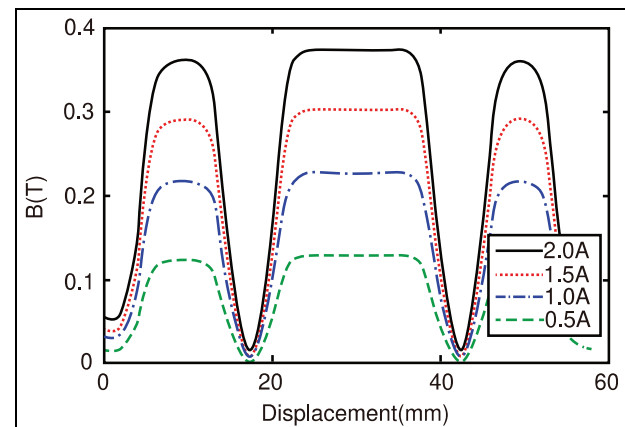


Figure 9. The magnetic induction intensity distribution of the annular damping channel under different currents.

with the excitation current. The greater the current, the higher the magnetic induction intensity.

The distribution of the axial magnetic induction intensity at the center of the cross-section of the annular damping channel under different excitation currents is shown in Figure 9. The magnetic induction intensity can reach 0.38 T in the effective area of the annular damping channel, while it is very low or even zero in the non-effective area.

Parameter matching for damper valve system

If the pressure matching between the MR piston and the bottom valve is unreasonable, the cavitation effect of the damper may occur. The cavitation effect refers to the phenomenon that when the static pressure is lower than the steam pressure, part of the damping fluid will

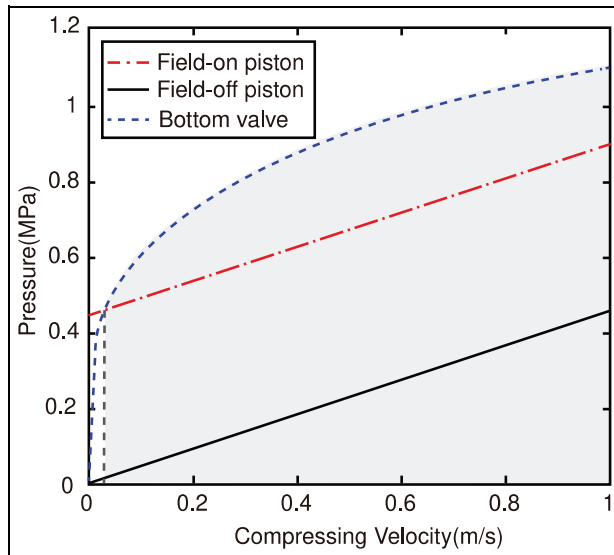


Figure 10. Relationships between the pressures of the bottom valve and the MR piston and the compression velocity of the damper.

transform from fluid to gas, resulting in the failure of the damping force. However, a small pressure can transform the gaseous damping fluid into a liquid state. Besides, the process will be accompanied by severe impacts and generate loud noises, which may cause damage to the internal structure of the damper. If the temperature gradually increases, the steam pressure of the damping fluid increases and cavitation effect is more likely to occur, which is a severe challenge for MR damper with high heat generation. In order to avoid the cavitation effect, it is necessary to ensure that the pressure generated by the MR piston head during the compression stroke is lower than the pressure generated by the bottom valve. In this study, the reasonable pressure matching between the MR piston and the bottom valve is realized by changing the area of the normally open throttle and the equivalent thickness of the stacked valve plate. After matching the valve system, the relationships between the pressures of the bottom valve and the MR piston and the compression velocity of the damper are shown in Figure 10.

As shown in Figure 10, with the increase of the relative velocity of the low-friction MR damper, the pressures generated by the MR piston with field on and off increase linearly. After the valve system is matched, the pressure generated by the bottom valve is generally greater than the pressure generated by the MR piston with field on and off, as shown in the shadow part of Figure 10. This area covers almost the entire velocity range. Only when the velocity is less than 0.05 m/s, it does not meet the pressure requirement. However, due to the small expected damping force of the damper at extremely low velocities, the expected output pressure of the MR piston is relatively low. Therefore, the pressure requirement of the bottom valve can be appropriately reduced at low velocity.

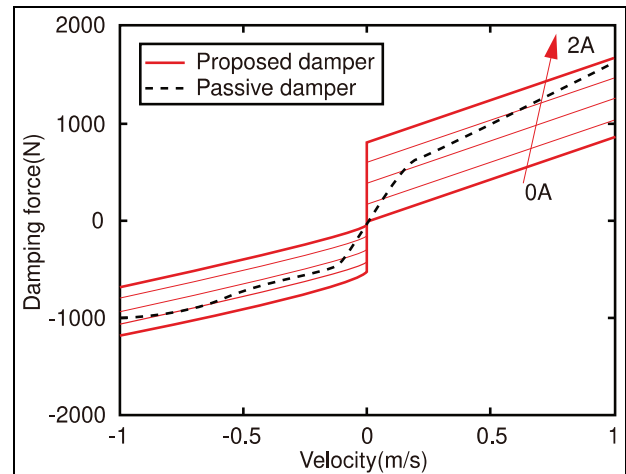


Figure 11. Comparison of the relationship of damping force with velocity between proposed low-friction MR damper and passive damper.

The comparison of the relationship of the damping force with the velocity between the low-friction MR damper and the passive damper is shown in Figure 11. The low-friction MR damper can generate a wide range of controllable damping force in both compression and rebound strokes, completely covering the mechanical characteristics of the passive damper. The damping force changes uniformly with the uniform increase of current. When the relative speed of the damper is 1 m/s, the controllable range of the compression damping force and rebound damping force is -684.2 to -1185 N and 864.7 to 1670 N, respectively. This range includes the peak compression and rebound damping forces of the passive damper, which are -1024 and 1637 N, respectively.

Test and analysis

Test system

In order to verify the mechanical properties of the proposed low-friction MR damper in the entire working velocity range, 0–1 m/s, a low-friction MR damper mechanical property test system was built as shown in Figure 12. The vibration excitation system used is the SAGINOMIYA vertical vibration test system, which is mainly composed of a computer, a control cabinet, a cooling pump, and an electronically controlled hydraulic vibration excitation table. The vibration excitation system can provide the vibration excitation of displacement waveforms such as sine wave, square wave, and triangular wave with a maximum load of 47 kN, a frequency range of 0.05–50 Hz, and a stroke of ± 147 mm. The controllable current source provides continuously adjustable excitation current at both ends of the MR damper coil to change the damping force of the damper. The force sensor above the system and the displacement sensor built in the exciter collect relevant data

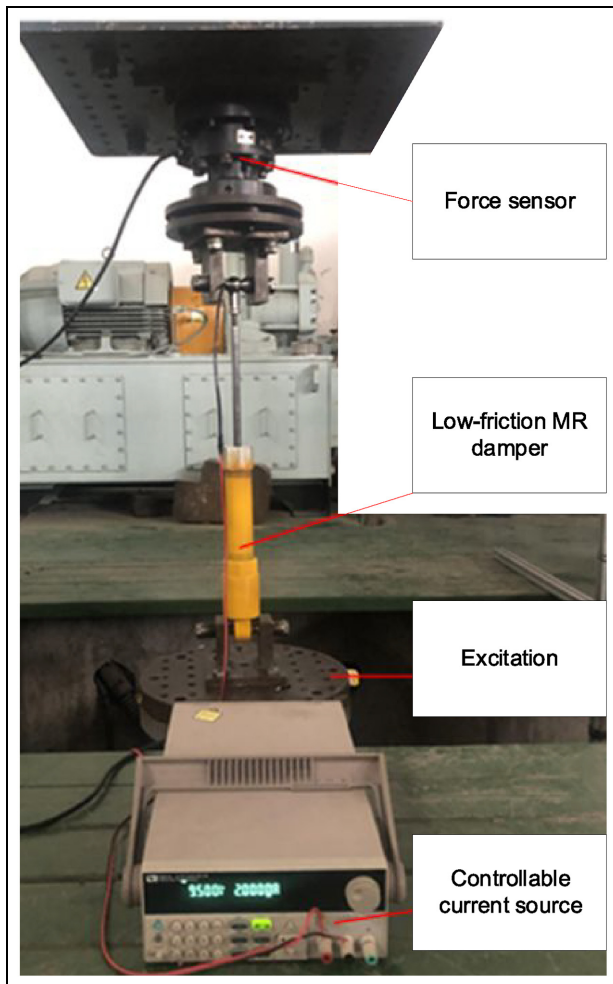


Figure 12. Test system for low-friction MR damper mechanical properties.

to obtain the damping properties of the low-friction MR damper under different excitation velocities and excitation currents.

Mechanical properties

During the damping characteristic test, a sinusoidal displacement excitation with a frequency of 1 Hz and an amplitude of 50 mm was applied to the low-friction MR damper with an inflation pressure of 0.6 MPa. Gradually applying excitation currents from 0 to 2 A at intervals of 0.5 A, the damping force-displacement curve and damping force-velocity curve of the low-friction MR damper were obtained as shown in Figure 13.

As shown in Figure 13(a), the shape of the damping force vs. displacement curves measured in the test are relatively plump, and no cavitation effect occurs during the compression reversing process. Therefore, it is reasonable to set the inflation pressure of the proposed low-friction MR damper to 0.6 MPa, which is much lower than the conventional MR damper. However, there is still a certain gap between the damping force amplitude obtained from the test and the simulation,

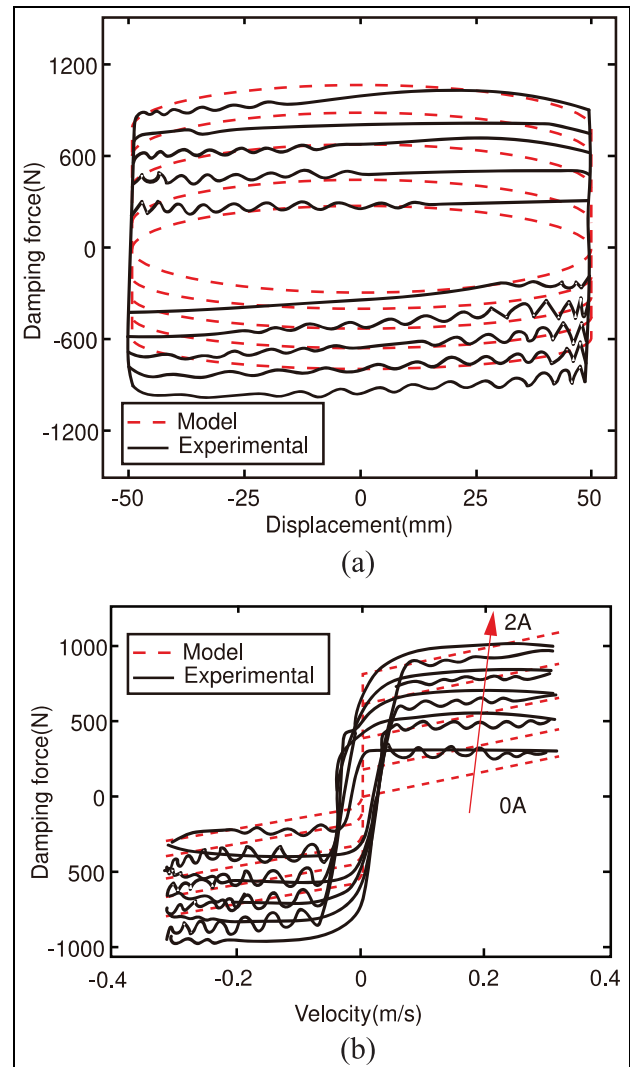


Figure 13. The damping force comparison between the simulation and experiment when the low-friction MR damper is under a sinusoidal displacement excitation with a frequency of 1 Hz and an amplitude of 50 mm: (a) damping force vs. displacement and (b) damping force vs. velocity.

mainly reflected in the large damping force errors at low speed and during the compression stroke. As shown in Figure 13(b), the damping forces of the low-friction MR damper measured in the test are relatively large at low speed. According to the mathematical model of damping force, it can be inferred that the reason for the large damping force at low speed in the rebound stroke is that the width of the annular damping channel of the actually machined MR piston is relatively small and the spring stiffness of the one-way valve is relatively large, which requires a large pressure to push the one-way valve open. The reason for the large deviation of the damping force in the compression stroke is that the equivalent thickness of the processed stacked valve plate exceeded the theoretical value by 0.1 mm, resulting in an increase in the stiffness of the compression valve and an increase in the minimum pressure required to open the compression valve.

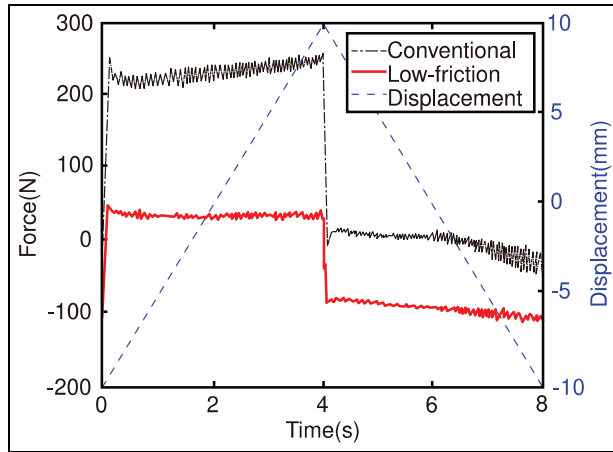


Figure 14. The curves of force versus time and displacement versus time of conventional and proposed low-friction MR dampers under low-speed triangular wave displacement excitation.

To verify the impact of the inflation pressure on the frictional force of the MR damper, this section ignores the non-pressure factors affecting the damper and compares the low-friction MR damper with an inflation pressure of 0.6 MPa proposed in this study and the conventional monotube MR damper with an inflation pressure of 2 MPa. Applying triangular wave excitation with a speed of 5 mm/min, amplitude of 10 mm, and frequency of 0.125 Hz to the MR damper test system to obtain the force and displacement data of the MR damper. According to QC/T 545-1999 *Bench test methods for Telescopic Shock Absorbers Used on Car*, during the test, the relative velocity of the damper is so small that its damping force can be ignored, and only gas elastic force and frictional force need to be considered. The force and displacement characteristic curves of the MR damper within a cycle are shown in Figure 14.

At the midpoint of the compression stroke, the gas pressure and the frictional force are in the same direction, so the data measured by the force sensor is the sum of the two. At the midpoint of the rebound stroke, the gas pressure and the frictional force are opposite, so the data measured by the sensor is the difference between the two. The gas pressure and friction amplitude at the midpoint of the two strokes can be regarded as constant. Therefore, the frictional forces of the low-friction MR damper and the conventional MR damper are obtained to be 62.5 and 107.4 N, respectively.

In summary, the low-friction MR damper proposed in this study has a low inflation pressure of only 0.6 MPa, and no cavitation effect was observed in the test. The frictional force is only 62.5 N, which is significantly lower than conventional MR damper with high inflation pressure.

System performance simulation

In order to investigate the effect of reducing the frictional force of MR damper on the damping

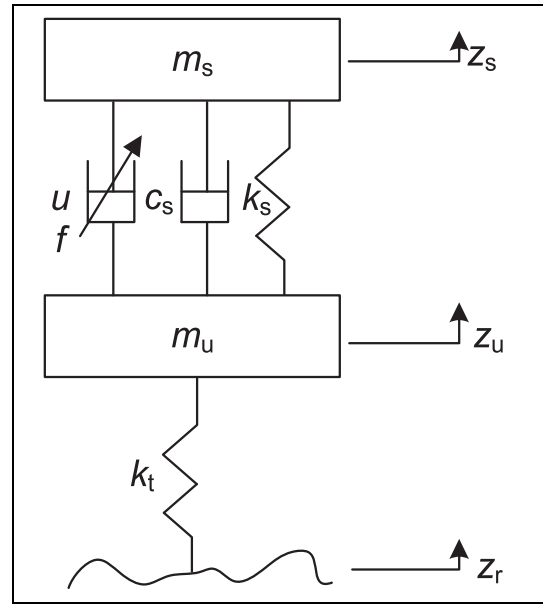


Figure 15. Unified model of the 1/4 vehicle passive/semi-active suspension.

performance of passive suspension and semi-active suspension, a 1/4 vehicle model was established. For simplicity, the sprung mass acceleration is used as the evaluation index of ride comfort and the dynamic tire load is used as the evaluation index of handling stability.

Modeling of the 1/4 vehicle suspension system dynamics

Figure 15 illustrates a unified model for 1/4 vehicle passive and semi-active suspension. In Figure 15, m_s is the sprung mass; m_u is the unsprung mass; k_t is the stiffness of the tire; c_s is damping of the passive damper; Z_s , Z_u , and Z_r are the displacements of the sprung mass, unsprung mass, and road excitation, respectively; k_s is the stiffness of the elastic element of the suspension, which is equal to the sum of the stiffness of the suspension spring and the damper limit block; and u is the force input of the semi-active suspension. To reduce the number of inputs, the frictional force f is merged into the semi-active suspension force input u . For passive suspension, u is equal to f . While, for semi-active suspension, c_s is equal to 0, and u is the sum of the damping force and frictional force. When a car is driving on harsh roads or roads with speed bumps or dents at high speed, the suspension limit block may participate in buffering, reducing the probability of the damper hitting the top and bottom, avoiding rigid collisions between relatively moving components, and thus improving the service life of the dampers and wheels. Therefore, the passive/semi-active suspension model of the 1/4 vehicle in this study introduces suspension limit blocks, which limited the stroke of the damper to ± 80 mm. The maximum compression of the suspension

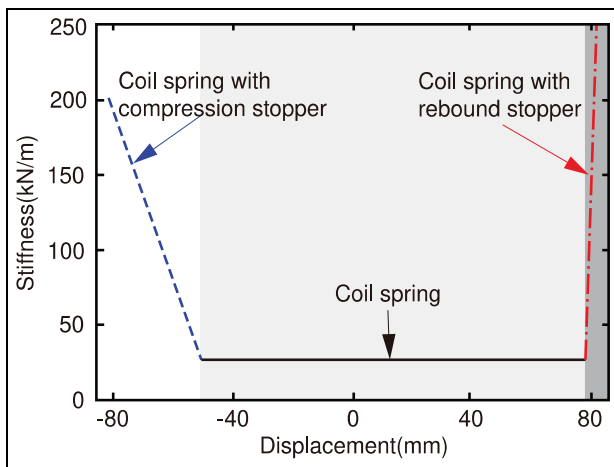


Figure 16. Stiffness of elastic elements of suspension at different positions.

limit block is 40 mm, which simulates the deterioration of the vehicle performance under extreme conditions when the damper piston collided with the limit block, and thus the effect of suspension deflection on the performance of the 1/4 vehicle was fully utilized. While, the maximum compression of the rebound limit block is 3 mm. Figure 16 shows the total stiffness of the elastic elements of the 1/4 vehicle passive/semi-active suspension at different positions.

The state space equation of the unified model of the 1/4 vehicle passive/semi-active suspension system in Figure 15 can be expressed as:

$$\begin{cases} \dot{\mathbf{X}} = \mathbf{AX} + \mathbf{Bu} + \mathbf{L}_1 w \\ \mathbf{Y} = \mathbf{CX} + \mathbf{Du} + \mathbf{L}_2 w \end{cases} \quad (25)$$

where, $\mathbf{X} = [z_s \dot{z}_s z_u \dot{z}_u]^T$ is the input variable; $\mathbf{Y} = [\ddot{z}_s z_s - z_u k_t (z_u - z_t)]^T$ is the output variable, which is the acceleration of the sprung mass and dynamic load of tire; w is the road input z_r ; and

$$\mathbf{A} = \begin{bmatrix} 0 & 1 & 0 & 0 \\ \frac{-k_s}{m_s} & \frac{-c_s}{m_s} & \frac{k_s}{m_s} & \frac{c_s}{m_s} \\ 0 & 1 & 0 & 1 \\ \frac{k_s}{m_u} & \frac{c_s}{m_u} & \frac{-(k_t + k_s)}{m_u} & \frac{-c_s}{m_u} \end{bmatrix}; \mathbf{B} = \begin{bmatrix} 0 \\ \frac{-1}{m_s} \\ 0 \\ \frac{1}{m_u} \end{bmatrix}; \mathbf{L}_1 = \begin{bmatrix} 0 \\ 0 \\ 0 \\ \frac{k_t}{m_u} \end{bmatrix}$$

$$\mathbf{C} = \begin{bmatrix} \frac{-k_s}{m_s} & \frac{-c_s}{m_s} & \frac{k_s}{m_s} & \frac{c_s}{m_s} \\ 1 & 0 & -1 & 0 \\ 0 & 0 & k_t & 0 \end{bmatrix}; \mathbf{D} = \begin{bmatrix} -\frac{1}{m_s} \\ 0 \\ 0 \end{bmatrix}; \mathbf{L}_2 = \begin{bmatrix} 0 \\ 0 \\ 0 \\ -k_t \end{bmatrix}.$$

In this study, the skyhook damping control is used as the control method for the semi-active suspension. However, considering the boundedness of the MR damper output force in engineering applications, it is necessary to limit the upper and lower limits of the ideal skyhook control force u_{sky} :

Table 2. Dynamic model parameters of simulated vehicle.

Symbol	Specification	Value	Unit
m_s	Sprung mass	365.8	kg
m_u	Unsprung mass	60.2	kg
k_t	Tire stiffness	232,000	N/m

$$u_{sky} = \begin{cases} F_{max} & |u_{sky}| \geq |F_{max}| \\ u_{sky} & |F_{min}| < |u_{sky}| < |F_{max}| \\ F_{min} & |u_{sky}| \leq |F_{min}| \end{cases} \quad (26)$$

where, F_{min} and F_{max} are the minimum and maximum damping forces that can be output by the MR damper, namely the zero-field damping force and the damping force output by MR damper when the excitation current reaches the maximum value of 2 A. F_{min} and F_{max} can be calculated by the established MR damper mathematical model. u_{sky} is the ideal skyhook control force, which can be expressed as:

$$u_{sky} = \begin{cases} c_{sky} \dot{z}_s \dot{z}_s (\dot{z}_s - \dot{z}_u) \geq 0 \\ 0 & \dot{z}_s (\dot{z}_s - \dot{z}_u) < 0 \end{cases} \quad (27)$$

where, c_{sky} is the skyhook damping coefficient.

Analysis of the influence of frictional force on suspension performance

The parameters of the simulated vehicle model are listed in Table 2. The low-pass filtered white noise signal satisfying the Gaussian distribution is used to simulate random road input. The road grade is B and the driving speed is 60 km/h. The simulation results of the performance of the passive suspension and the semi-active suspension with skyhook damping control affected by the friction of the damper are shown in Figure 17.

As shown in Figure 17, with the increase of frictional force, both the sprung mass acceleration RMS values of passive suspension and semi-active suspension gradually increase, and the ride comfort of the vehicle becomes worse. When the suspension works under the ideal condition without friction, compared to the RMS value of the sprung mass acceleration of passive suspension, which is 0.39 m/s^2 , the semi-active suspension is only 0.195 m/s^2 , a 50% reduction. In addition, compared to no friction condition, when the frictional force is 100 N, the RMS value of the passive suspension sprung mass acceleration is 0.53 m/s^2 , increased by 36 %. While the RMS value of the semi-active suspension sprung mass acceleration is 0.38 m/s^2 , increased by 95%. The comparison indicates that the sprung mass acceleration of the semi-active suspension has a higher

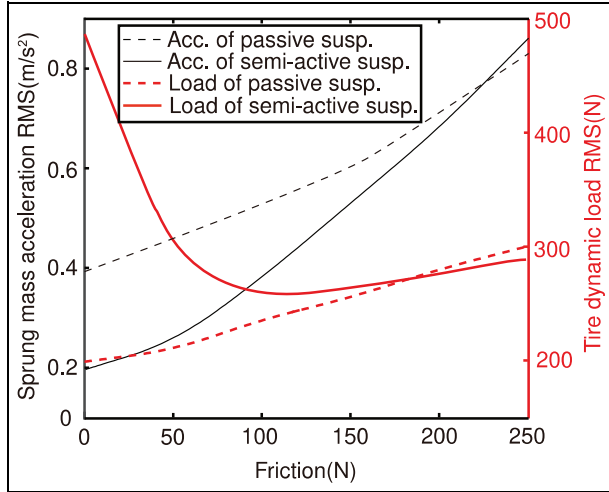


Figure 17. Influence of frictional force on the sprung mass acceleration and dynamic tire load of passive and semi-active suspension.

sensitivity to the frictional force, which means the frictional force has a greater influence on the damping performance of the MR semi-active suspension.

According to Figure 17, the RMS value of the dynamic tire load of the passive suspension increases with the increase of the frictional force, resulting in a decrease in the adhesion ability of the tire to the ground and a decrease in the vehicle handling stability. While, the RMS value of the dynamic tire load of the semi-active suspension first decreases and then slowly increases with the increase of the frictional force, indicating that the vehicle handling stability first increases and then decreases. This is because the frictional force makes the skyhook damping control unable to exert its characteristic of optimizing ride comfort at the cost of reducing the handling stability.

Figure 18 shows the time domain responses of the sprung mass acceleration and dynamic tire load of passive and semi-active suspensions with frictional force of 0 and 100 N. Figure 18(a) shows that the frictional force causes an increase in the amplitude of the sprung mass acceleration of both passive and semi-active suspensions, reducing the ride comfort of vehicle. Figure 18(b) shows that the frictional force increases the dynamic tire load of the passive suspension and deteriorates the vehicle handling stability. However, the frictional force significantly reduces the dynamic tire load of the semi-active suspension with skyhook damping control, which is consistent with the results in Figure 17. For more clarity, Figure 18(c) shows the RMS values of the sprung mass acceleration and dynamic tire load of passive and semi-active suspensions with frictional force of 0 and 100 N, which illustrates the same conclusion as shown in Figure 18(a) and (b).

Figure 19 shows the frequency domain responses of sprung mass acceleration and dynamic tire load of passive and semi-active suspensions with frictional force of

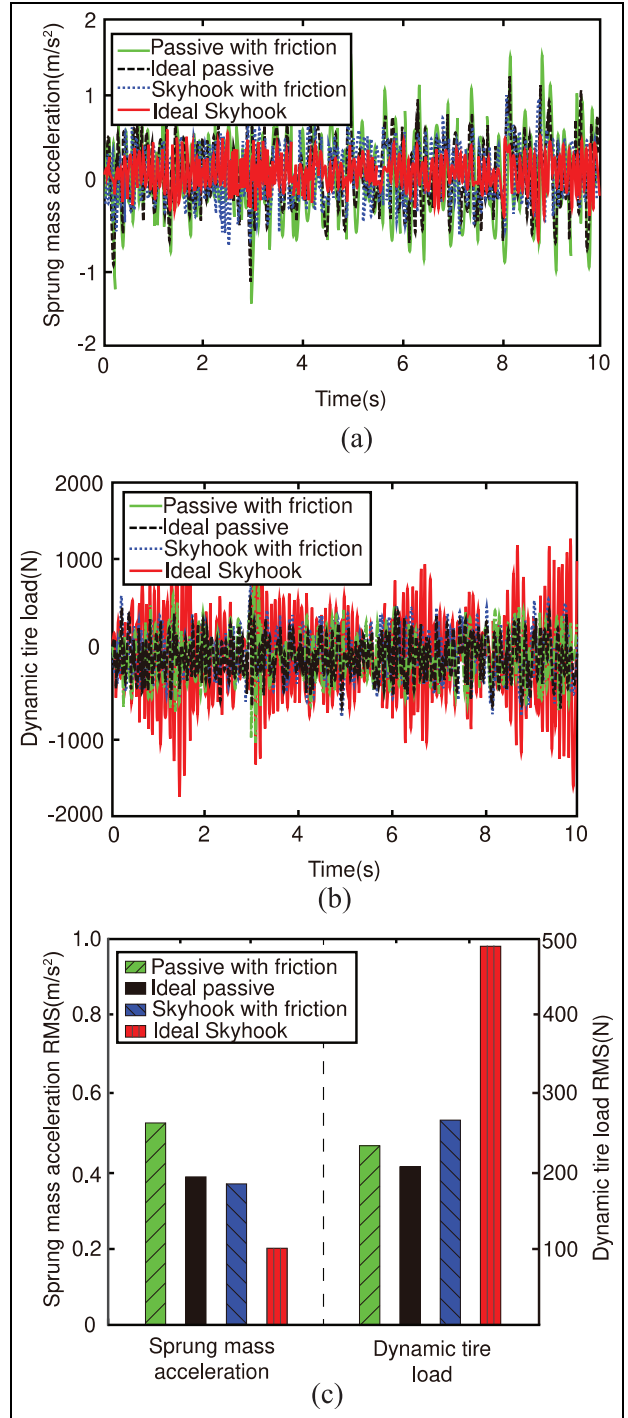


Figure 18. Time domain responses of passive and semi-active suspensions with frictional forces of 0 and 100 N: (a) sprung mass acceleration, (b) dynamic tire load, and (c) RMS value.

0 and 100 N, respectively. Figure 19(a) shows that the frictional force seriously deteriorates the amplitude of the sprung mass acceleration in the middle frequency range between the first- and second-order resonance frequencies of the passive suspension, as well as in the high frequency range above the second-order resonance frequency. Although the frictional force reduces the second-order resonance peak value of the sprung mass

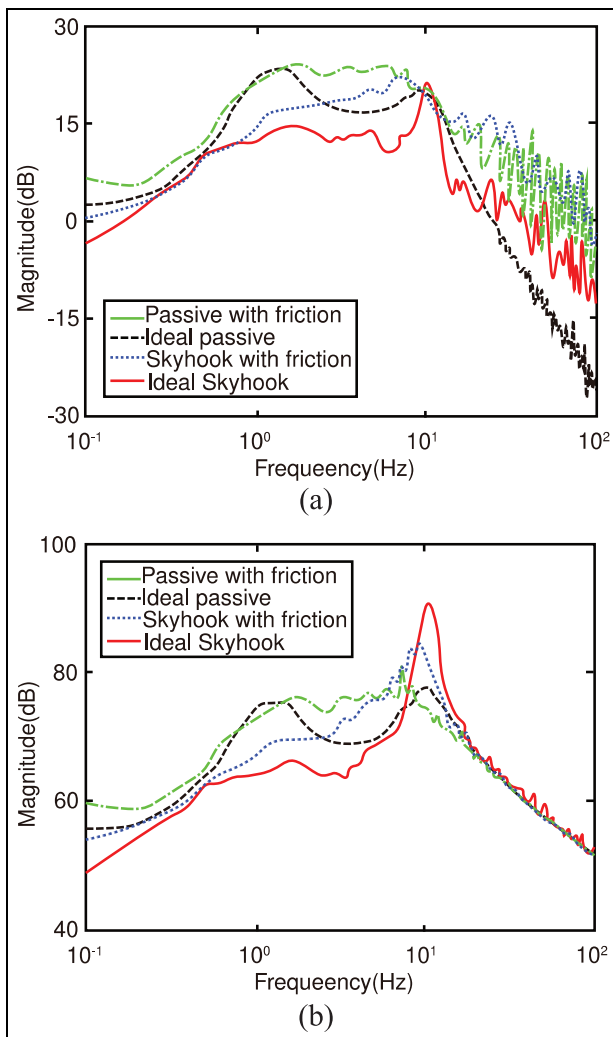


Figure 19. Frequency domain responses of passive and semi-active suspensions with frictional forces of 0 and 100 N: (a) sprung mass acceleration and (b) dynamic tire load.

acceleration of the semi-active suspension by 1 dB, it seriously deteriorates the sprung mass acceleration in the frequency band near the first-order resonance frequency, the middle frequency band between the first- and second-order resonance frequencies, and the high frequency band above the second-order resonance frequency. Thereby, the frictional force reduces the ride comfort of the vehicle. Figure 19(b) shows that the frictional force deteriorates the amplitude of the dynamic tire load at the middle frequency band of both passive and semi-active suspensions but reduces the second-order resonance peak value of the semi-active suspension by about 6 dB, which is consistent with illustration of Figure 18(b) that the frictional force improves the handling stability of the semi-active suspension with skyhook damping control.

In summary, for passive suspension, friction has a deteriorating effect on ride comfort and handling stability of the vehicle; while, for semi-active suspension, the

ride comfort of the vehicle decreases with the increase of frictional force, and the handling stability of the vehicle increases when the friction is small, but gradually decreases when the friction exceeds a certain threshold, such as 100 N in this study. It can be seen that reducing the friction of MR damper can effectively improve the performance of semi-active suspension. Compared to the traditional MR damper, the proposed low-friction MR damper has extremely low friction, which is beneficial to improve the performance of the semi-active suspension based on MR damper.

Conclusion

In this paper, a low-friction MR damper is proposed to address the issue of large frictional force in traditional monotube MR dampers, which reduces friction by reducing inflation pressure. An experimental setup was established and the specific influence of frictional force on suspension performance was investigated. Based on the research results, conclusions can be drawn as:

1. Compared with other monotube MR dampers, the proposed low-friction MR damper has introduced a bottom valve structure, using stacked valve plates instead of the slotted valve plates, which increases the pressure generated by the bottom valve in the low-velocity zone.
2. The parameter optimization of the key structure of the MR piston head has reduced the manufacturing cost and improved the response speed of the MR damper. The parameter matching of the bottom valve based on the controllable force range of the MR piston has avoided the cavitation effect.
3. The proposed low-friction MR damper has reduced the inflation pressure to 0.6 MPa, and no cavitation effect occurs during the compression reversing process. Compared with the conventional monotube MR damper with an inflation pressure of 2 MPa, the frictional force of the low-friction MR damper has been reduced from 107.4 to 62.5 N.
4. For passive suspension, the frictional force has a deteriorating effect on the ride comfort and handling stability of the vehicle. For semi-active suspension, on the one hand, the frictional force significantly deteriorates the ride comfort of the vehicle, reducing the vibration isolation advantage of the semi-active suspensions. On the other hand, low friction improves the handling stability of the vehicle, but when a certain threshold is exceeded, 100 N in this study, the handling stability of the vehicle gradually deteriorates. Therefore, reducing the frictional force of the MR damper can effectively improve the performance of the semi-active suspension.

Declaration of conflicting interests

The author(s) declared no potential conflicts of interest with respect to the research, authorship, and/or publication of this article.

Funding

The author(s) disclosed receipt of the following financial support for the research, authorship, and/or publication of this article: The authors wish to acknowledge the National Natural Science Foundation of China (Grant No. 52272392) and the Fundamental Research Funds for the Central Universities of China (Grant Nos. PA2021GDSK0076 and JZ2023YQTD0073) for the financial support of this research.

ORCID iDs

Weihan Li  <https://orcid.org/0000-0003-0249-9020>
 Xianxu 'Frank' Bai  <https://orcid.org/0000-0003-4477-8335>

References

- East W, Turcotte J, Plante J-S, et al. Experimental assessment of a linear actuator driven by magnetorheological clutches for automotive active suspensions. *J Intell Mater Syst Struct* 2021; 32(9): 955–970.
- Karimi HR. *Vibration control and actuation of large-scale systems*. London: Academic Press, 2020.
- Oh JS, Jeon K, Kim GW, et al. Dynamic analysis of semi-active MR suspension system considering response time and damping force curve. *J Intell Mater Syst Struct* 2021; 32(13): 1462–1472.
- Theunissen J, Tota A, Gruber P, et al. Preview-based techniques for vehicle suspension control: a state-of-the-art review. *Annu Rev Control* 2021; 51: 206–235.
- Yang J, Ning D, Sun S, et al. A semi-active suspension using a magnetorheological damper with nonlinear negative-stiffness component. *Mech Syst Signal Process* 2021; 147: 107071.
- Bai X-XF and Yang S. Hybrid controller of magnetorheological semi-active seat suspension system for both shock and vibration mitigation. *J Intell Mater Syst Struct* 2019; 30(11): 1613–1628.
- Tudon-Martínez JC, Hernandez-Alcantara D, Amezcua-Brooks L, et al. Magneto-rheological dampers-model influence on the semi-active suspension performance. *Smart Mater Struct* 2019; 28(10): 105030.
- Eshgar H, Ahmadi Nadooshan A and Raisi A. An overview on properties and applications of magnetorheological fluids: Dampers, batteries, valves and brakes. *J Energy Storage* 2022; 50: 104648.
- Narwade P, Deshmukh R, Nagarkar M, et al. Improvement of ride comfort in a passenger car using magneto-rheological (MR) damper. *J Vib Eng Tech* 2022; 10(7): 2669–2676.
- Xu X, Liu H, Jiang X, et al. Uncertainty analysis and optimization of quasi-zero stiffness air suspension based on polynomial chaos method. *Chin J Mech Eng* 2022; 35(1): 93.
- Morales AL, Nieto AJ, Chicharro JM, et al. A semi-active vehicle suspension based on pneumatic springs and magnetorheological dampers. *J Vib Control* 2018; 24(4): 808–821.
- Kandavalli SR, Cruze D, Ram A, et al. Analytical investigation of MR damper for vibration control: a review. *J Appl Eng Sci* 2021; 11(1): 49–52.
- Mata GT, Mokenapalli V and Krishna H. Performance analysis of MR damper based semi-active suspension system using optimally tuned controllers. *Proc IMechE, Part D: J Automobile Engineering* 2021; 235(10–11): 2871–2884.
- Si Z, Bai XF, Qian L, et al. Principle and control of active engine mount based on magnetostrictive actuator. *Chin J Mech Eng* 2022; 35(1): 146.
- Wang D, Wang B, Zi B, et al. Development and control of a magnetorheological damper-based brake pedal simulator for vehicle brake-by-wire systems. *Chin J Mech Eng* 2022; 35(1): 136.
- Tell S, Andersson A, Najafi A, et al. Real-time hybrid testing for efficiency assessment of magnetorheological dampers to mitigate train-induced vibrations in bridges. *Int J Rail Transp* 2022; 10(4): 436–455.
- Willey CL, Chen VW, Scalzi KJ, et al. A reconfigurable magnetorheological elastomer acoustic metamaterial. *Appl Phys Lett* 2020; 117(10): 104102.
- Deng H, Gao Y, Hu R, et al. Self-sensing automotive magnetorheological dampers for low frequency vibration. *Smart Mater Struct* 2021; 30(11): 115015.
- Ma T, Bi F, Wang X, et al. Optimized fuzzy skyhook control for semi-active vehicle suspension with new inverse model of magnetorheological fluid damper. *Energies* 2021; 14(6): 1674.
- Dong L, Zhao R, Luo B, et al. Design of a new damper based on magnetorheological fluids. *Int J Appl Electromagn Mech* 2019; 59(1): 357–366.
- Jiang M, Rui X, Yang F, et al. Multi-objective optimization design for a magnetorheological damper. *J Intell Mater Syst Struct* 2022; 33(1): 33–45.
- Yoon D-S, Kim G-W and Choi S-B. Response time of magnetorheological dampers to current inputs in a semi-active suspension system: Modeling, control and sensitivity analysis. *Mech Syst Signal Process* 2021; 146: 106999.
- Jeyasenthil R, Yoon DS and Choi S-B. Response time effect of magnetorheological dampers in a semi-active vehicle suspension system: Performance assessment with quantitative feedback theory. *Smart Mater Struct* 2019; 28(5): 054001.
- Strecker Z, Roupec J, Mazurek I, et al. Design of magnetorheological damper with short time response. *J Intell Mater Syst Struct* 2015; 26(14): 1951–1958.
- Yoon D-S, Park Y-J and Choi S-B. An eddy current effect on the response time of a magnetorheological damper: Analysis and experimental validation. *Mech Syst Signal Process* 2019; 127: 136–58.
- Yan J and Dong L. Design and modeling of a magnetorheological damper with double annular damping gap. *J Intell Mater Syst Struct* 2023; 34(8): 976–989.
- Hu G, Wu L, Deng Y, et al. Optimal design and performance analysis of magnetorheological damper based on multiphysics coupling model. *J Magn Magn Mater* 2022; 558(15): 169527.

28. Liu S, Feng L, Zhao D, et al. The development of an outer multi-pole magneto-rheological damper with high dynamic range of damping force. *Smart Mater Struct* 2018; 27(11): 115025.
29. Gaoyu L, Fei G and Wei-Hsin L. Magnetorheological damper with multi-grooves on piston for damping force enhancement. *Smart Mater Struct* 2021; 30(2): 025007.
30. Liu G, Gao F and Liao W-H. Shape optimization of magnetorheological damper piston based on parametric curve for damping force augmentation. *Smart Mater Struct* 2022; 31(1): 015027.
31. Kubík M, Machacek O, Strecker Z, et al. Design and testing of magnetorheological valve with fast force response time and great dynamic force range. *Smart Mater Struct* 2017; 26(4): 047002.
32. Bai X-XF and Li C-X. Precise real-time hysteretic force tracking of magnetorheological damper. *Smart Mater Struct* 2020; 29(10): 104002.
33. Gołdasz J and Sapiński B. *Insight into magnetorheological shock absorbers*. Switzerland: Springer International Publishing, 2015.
34. Phillips RW. *Engineering applications of fluids with a variable yield stress*. Berkeley: University of California, 1969.
35. Brown TH. *Marks' calculations for machine design*. New York, NY: McGraw-Hill, 2005.

Appendix A

Figure A1 shows the relationship between the yield stress of MR fluid and the magnetic induction intensity measured experimentally.

Table A1 shows the polynomial fitting coefficients of the yield stress of MR fluid and the maximum deflection coefficient.

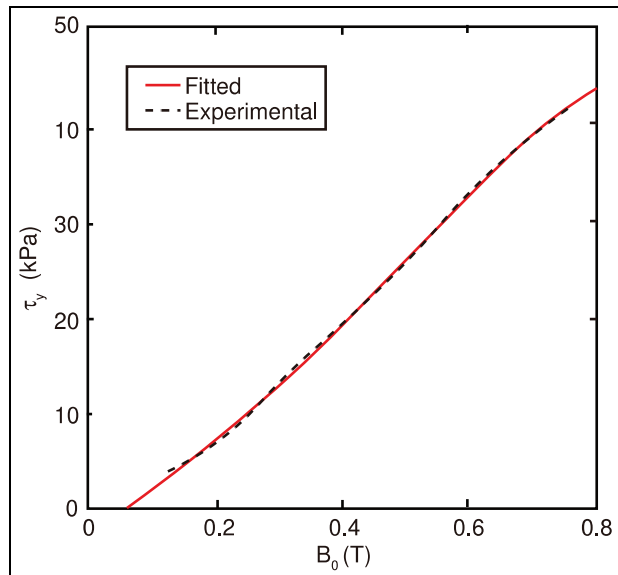


Figure A1. The relationship between yield stress of MR fluid and magnetic induction intensity.

Table A1. Polynomial fitting coefficients of τ_y and C_6 .

Term	Coefficient	Value
τ_y	α_0	-2.636
	α_1	48.94
	α_2	-17.85
	α_3	118.9
	α_4	-103.1
C_6	β_0	0.2513
	β_1	-0.5433
	β_2	0.3565
	β_3	-0.07216
	β_4	0.00502